Journal of Colloid and Interface Science 459 (2015) 224–229

Contents lists available at ScienceDirect

Journal of Colloid and Interface Science

journal homepage: www.elsevier.com/locate/jcis

Solvothermal synthesis and upconversion properties of about 10 nm orthorhombic LuF_3: Yb^{3+}, Er^{3+} rectangular nanocrystals

Guotao Xiang [a,b], Jiahua Zhang [a,*], Zhendong Hao [a], Xia Zhang [a], Guo-Hui Pan [a], Li Chen [c], Yongshi Luo [a], Shaozhe Lü [a], Haifeng Zhao [a]

[a] State Key Laboratory of Luminescence and Applications, Changchun Institute of Optics, Fine Mechanics and Physics, Chinese Academy of Sciences, 3888 Eastern South Lake Road, Changchun 130033, China
[b] Graduate School of Chinese Academy of Sciences, Beijing 100039, China
[c] School of Basic Sciences, ChangChun University of Technology, A1018 Huguang Road, Changchun 130012, China

GRAPHICAL ABSTRACT

Compared with YF_3 and α-$NaYF_4$ NCs, owning the similar size and the same doping levels of Yb^{3+} ions and Er^{3+} ions as LuF_3 NCs, the green UC emission of LuF_3 NCs is 18.7 times and 5.1 times stronger than that of YF_3 and α-$NaYF_4$ NCs respectively; the red UC emission of LuF_3 NCs is 13.2 times and 0.6 times stronger than that of YF_3 and α-$NaYF_4$ NCs respectively.

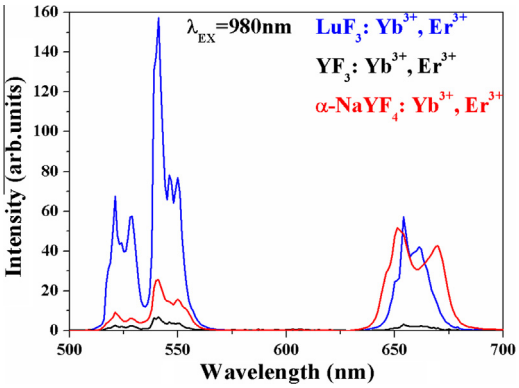

ARTICLE INFO

Article history:
Received 2 July 2015
Revised 8 August 2015
Accepted 13 August 2015
Available online 13 August 2015

Keywords:
LuF_3
Solvothermal process
Upconversion
Thermal effect

ABSTRACT

The Yb^{3+} and Er^{3+} codoped orthorhombic LuF_3 rectangular nanocrystals (NCs) with the size of about 10 nm were synthesized by a facile and effective solvothermal process. X-ray diffraction (XRD), transmission electron microscopy (TEM), high-resolution transmission electron microscopy (HRTEM), upconversion (UC) luminescence spectra and decay curves were used to characterize the resulting samples. Compared with YF_3 and α-$NaYF_4$ NCs, owning the similar size and the same doping levels of Yb^{3+} ions and Er^{3+} ions as LuF_3 NCs, the green UC emission of LuF_3 NCs is 18.7 times and 5.1 times stronger than that of YF_3 and α-$NaYF_4$ NCs respectively; the red UC emission of LuF_3 NCs is 13.2 times and 0.6 times stronger than that of YF_3 and α-$NaYF_4$ NCs respectively. Under 980 nm wavelength excitation, the decay curves of both $^4S_{3/2} \rightarrow {}^4I_{15/2}$ transition and $^4F_{9/2} \rightarrow {}^4I_{15/2}$ transition exhibit a single exponential function, resulting from the fast energy migrations among Yb^{3+} ions caused by the high concentration of Yb^{3+} ions (20 mol%). Meanwhile, at relatively low power density, the slopes of the linear plots between *log(I)* and *log(P)* for green UC and red UC are 1.7 and 1.9 respectively, which are less than 2 due to the quenching of

* Corresponding author.
E-mail address: zhangjh@ciomp.ac.cn (J. Zhang).

http://dx.doi.org/10.1016/j.jcis.2015.08.026

the thermal effect, indicating a two-photon process for them. At high power density, the slopes are decreased caused by the saturation effect. In addition, we proved the existence of the thermal effect by the pump power dependence of the intensity ratio of $^2H_{11/2} \rightarrow {}^4I_{15/2}$ transition to $^4S_{3/2} \rightarrow {}^4I_{15/2}$ transition.

1. Introduction

In the last decades, rare earth fluoride UC NCs have been studied for applications in many fields, such as displays, solar cells, lasers, biolabels and medical diagnosis [1–8]. Especially in biological fields, rare earth fluoride UC NCs have attracted more and more attention. Compared with conventional downconversion fluorescent materials like quantum dots and organic fluorescent dyes, UC NCs have the following advantages: great tissue penetration, low background fluorescence and high signal-to-noise ratio [9–14]. Among the various rare earth fluoride UC nanocrystal hosts, $NaLnF_4$ and LnF_3 are considered to be excellent hosts for activators due to their low phonon energy, which can provide low nonradiative relaxation and high luminescence efficiency [15–28]. Moreover, for application in vivo imaging, there are some rigorous requirements, such as small diameter and bright luminescence [29–31]. Binary fluoride LnF_3 nanostructure, a category of important rare earth fluoride compounds have attracted increasing attention because of their small diameter and bright luminescence.

To the best of our knowledge, YF_3 is the best host for UC emission among all of the binary fluoride NCs [32]. So far, however, many investigations have demonstrated that trivalent rare earth ions doped Lu-based compounds, such as Yb^{3+} and Ln^{3+} (Ln = Er^{3+}, Ho^{3+}, Tm^{3+}) codoped β-$NaLuF_4$, Yb^{3+} and Er^{3+} codoped Lu_2O_3 show stronger UC luminescence than that found for the correspond-ing Y-based compounds [33,34]. This may be due to Lu unique electronic state at the top of the valence, which results to the increase of the oscillator strength of the doped rare earth ions in the crystals, according to the intensity-borrowing mechanism proposed by Guillot-Noel et al. [35]. Therefore, LuF_3, owning the similar structure to YF_3, may be a more promising host for UC behavior than YF_3.

Herein, we report the synthesis of about 10 nm orthorhombic LuF_3: 20% Yb^{3+}, 2% Er^{3+} rectangular NCs by a solvothermal process. The UC emission spectra, decay times and the thermal effect caused by laser radiation have been investigated in detail. The UC mechanisms has been discussed. YF_3 and α-$NaYF_4$ NCs synthesized also by the solvothermal process, owning the similar size and the same doping levels of Yb^{3+} ions and Er^{3+} ions as LuF_3 NCs, were used to compare the UC performance of LuF_3 NCs. Results show LuF_3 NCs is an excellent host for UC with small size and a promising material for the application of biological fields.

2. Experimental

2.1. Chemicals

Analytical pure NaOH, NH_4F, HCl, methanol and ethanol were obtained from Beijing Chemical Reagent Company. Cyclohexane (analytical pure) were obtained from Tianjin Guangfu Chemical Reagent Company. Lanthanide oxides of SpecPure grade (Er_2O_3, Yb_2O_3, Y_2O_3, Lu_2O_3, 99.99%) were purchased from Yangkou state-run rare earth company. 1-Octadecene (ODE, 90%) and oleic acid (OA, 90%) were supplied by Alfa Aesar. All of the chemical reagents were used as received without further purification. $LnCl_3$ was prepared by dissolving the corresponding lanthanide oxides in hydrochloric acid.

2.2. Synthesis of $LnCl_3$ (Ln=Lu, Y, Yb, Er) precursors

In a typical synthesis, the corresponding lanthanide oxides of $LnCl_3$ were dissolved into dilute hydrochloric acid, resulting in the formation of a colorless solution of $LnCl_3$. After evaporation followed by drying at 100 °C for 12 h in vacuum conditions, a powder of $LnCl_3$ was obtained.

2.3. Synthesis of LuF_3: 20% Yb^{3+}, 2% Er^{3+} NCs

In a typical synthesis, 0.78 mmol $LuCl_3$, 0.2 mmol $YbCl_3$ and 0.02 mmol $ErCl_3$, were added to a 100 mL three-neck round-bottom flask with 15 mL oleic acid and 15 mL 1-octadecene. The solution was heated slowly to 140 °C under vacuum with magnetic stirring for 30 min and to remove residual water and oxygen. The temperature was lowered to 50 °C and the reaction flask placed under a gentle flow of argon. During this time a solution of 3 mmol NH_4F dissolved in 10 mL of methanol was prepared. Once the reaction reached 50 °C, the methanol solution was added and the resulting cloudy mixture was stirred for 30 min at 50 °C to evaporate methanol from the reaction mixture. Then the reaction temperature was increased to 310 °C as quickly as possible and maintained at this temperature for 90 min under the argon gas flow. Subsequently, the mixture was allowed to cool to room temperature. The NCs were precipitated by the addition of ethanol and isolated via centrifugation at 8000 rpm for 10 min. The resulting product was dispersed in a minimal amount of cyclohexane and precipitated with excess ethanol. The NCs were again isolated via centrifugation at 8000 rpm each time. The NCs were then dispersed in 10 mL of cyclohexane.

2.4. Synthesis of YF_3: 20% Yb^{3+}, 2% Er^{3+} NCs

The synthetic procedure was the same as that used to synthesize LuF_3: 20% Yb^{3+}, 2% Er^{3+} NCs, except 0.78 mmol $LuCl_3$ was replaced by 0.78 mmol YCl_3.

2.5. Synthesis of α-$NaYF_4$: 20% Yb^{3+}, 2% Er^{3+} NCs

In a typical procedure for the synthesis of α-$NaYF_4$: 20% Yb^{3+}, 2% Er^{3+} NCs, 0.78 mmol YCl_3, 0.2 mmol $YbCl_3$ and 0.02 mmol $ErCl_3$ were added to a 100 mL three-neck round-bottom flask containing ODE (15 mL) and OA (6 mL). The solution was magnetically stirred and heated to 140 °C for 30 min to form the lanthanide oleate complexes and remove residual water and oxygen. The temperature was then cooled to 50 °C with a gentle flow of argon gas through the reaction flask. Meanwhile, a solution of NH_4F (4 mmol) and NaOH (2.5 mmol) dissolved in methanol (10 mL) was added to the flask and the resulting mixture was stirred for 30 min to evaporate methanol from the reaction mixture; The temperature was then increased to 280 °C in an argon atmosphere for 90 min and then naturally cooled to room temperature. The resultant solid state products were precipitated by the addition of ethanol, collected by centrifugation, washed with ethanol three times, and finally redispersed in cyclohexane.

2.6. Characterization

Powder X-ray diffraction (XRD) data were collected using Cu Kα radiation (λ = 1.54056 Å) on a Bruker D8 advance diffractometer (Germany) equipped with a linear position-sensitive detector (PSD-50 m, M. Braun), operating at 40 kV and 40 mA with a step size of 0.01° (2θ) in the range of 20–75°. The transmission electron microscopy (TEM) and high-resolution transmission electron microscopy (HRTEM) images were performed using a JEOL JEM 2100 TEM (Japan) equipped with an electron diffractometer (ED), operated at an acceleration voltage of 200 kV. The UC spectra were measured using a FLS920 spectrometer (Edinburgh Instruments, UK) pumped with a power-controllable 980 nm diode laser. In lifetime measurements, an optical parametric oscillator (OPO) was used as an excitation source and the signals were detected by a Tektronix digital oscilloscope (TDS 3052, USA). The lifetimes are calculated by integrating the area under the corresponding decay curves with the normalized initial intensity.

3. Results and discussion

3.1. Structure and morphology

Fig. 1(a) shows the XRD patterns of the Yb^{3+} and Er^{3+} codoped LuF_3 NCs prepared through the solvothermal method. The positions and relative intensity of the diffraction peaks for the Yb^{3+} and Er^{3+} codoped LuF_3 NCs can be indexed well to the standard cards of the orthorhombic LuF_3 (JCPDS 32-0612) with space group *Pnma* (No. 62). No second phase is detected in XRD patterns, demonstrating that Yb^{3+} and Er^{3+} substitutions for Lu^{3+} sites have no effect on the phase structure of the orthorhombic LuF_3 host. Fig. 1(b) shows the TEM image of the as-prepared NCs. The dispersed particles present rectangular nanoplates and own good monodispersity. The corresponding HRTEM image shows clearly lattice fringes with interplanar spacing of 3.6 Å ascribed to the (101) plane of LuF_3 (see Fig. 1(c)). The histograms of lengths and widths distribution of the samples, obtained from measuring 200 particles randomly, are shown in Fig. 1d and Fig. S1, respectively. As depicted in the histograms, the average size of the NCs is determined to be about 9.9 nm × 5.4 nm.

3.2. Luminescence properties

Fig. 2 shows the UC luminescence spectrum of the LuF_3: 20% Yb^{3+}, 2% Er^{3+} NCs at room temperature under 980 nm wavelength excitation with an output power density of 6 mW mm^{-2}. As shown in Fig. 2, three distinct bands in the range of 500–700 nm are observed. The dominant green emissions ranging from 510 to 535 nm and from 535 to 570 nm are assigned to the $^2H_{11/2} \rightarrow {}^4I_{15/2}$ and $^4S_{3/2} \rightarrow {}^4I_{15/2}$ transitions, respectively; the red emission from 630 to 690 nm is attributed to the $^4F_{9/2} \rightarrow {}^4I_{15/2}$ transition.

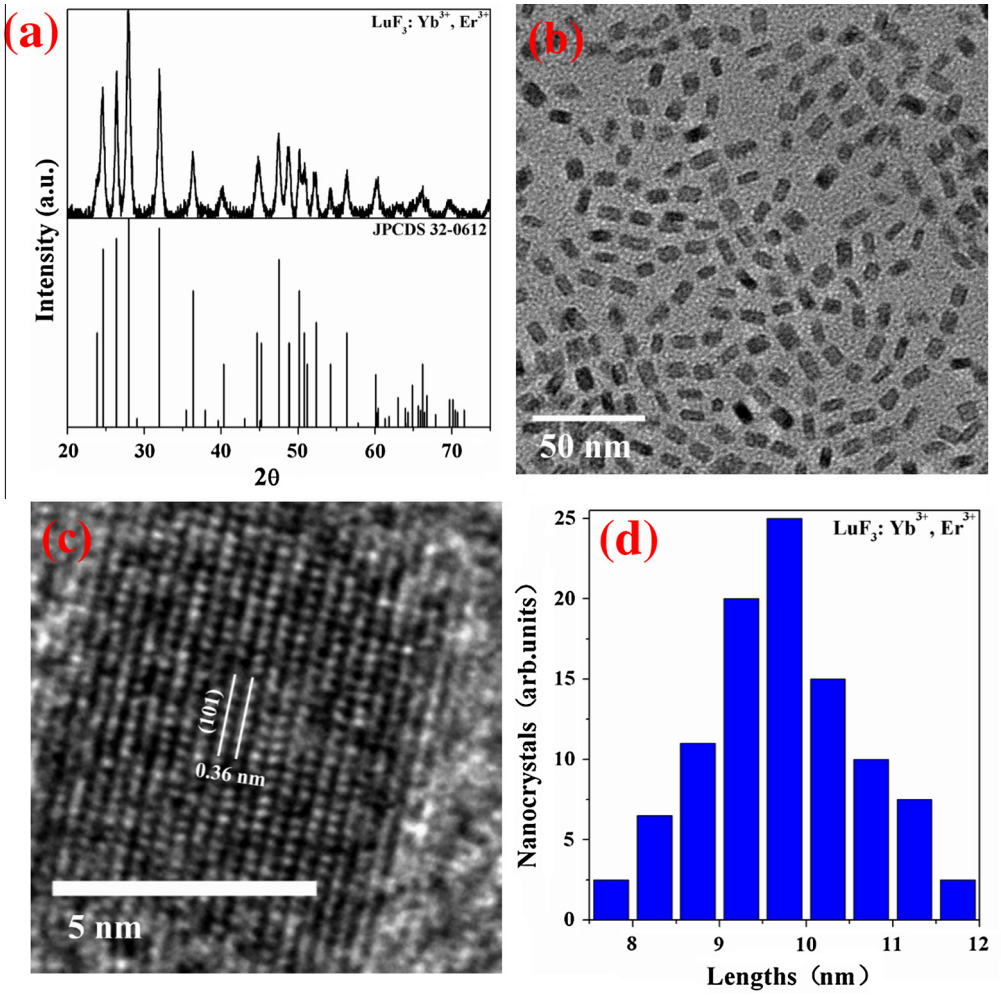

Fig. 1. (a) The XRD patterns, (b) the TEM image, (c) the HRTEM image and (d) the histogram of lengths distribution of LuF_3: Yb^{3+}, Er^{3+} NCs.

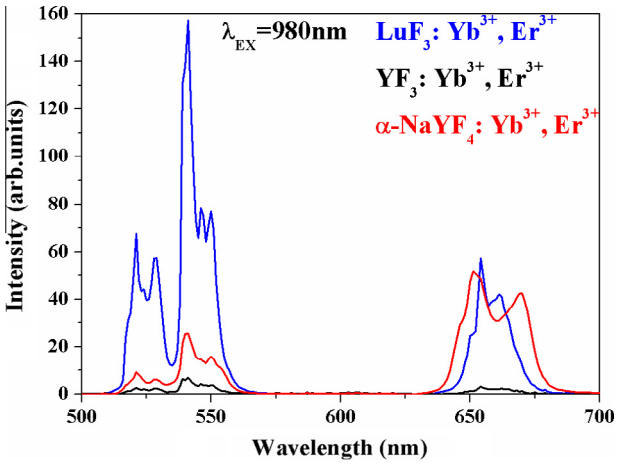

Fig. 2. The UC spectra of LuF_3: Yb^{3+}, Er^{3+} NCs, YF_3: Yb^{3+}, Er^{3+} NCs and α-$NaYF_4$: Yb^{3+}, Er^{3+} NCs under 980 nm excitation.

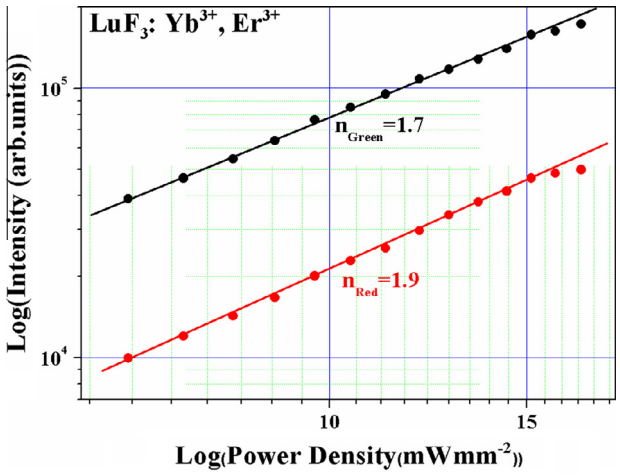

Fig. 4. The power dependence curves for the $^2H_{11/2}/^4S_{3/2} \rightarrow {}^4I_{15/2}$ transition and the $^4F_{9/2} \rightarrow {}^4I_{15/2}$ transition in LuF_3: Yb^{3+}, Er^{3+} NCs under 980 nm excitation wavelength.

In order to compare the UC properties, the YF_3 NCs (about 10 nm) and α-$NaYF_4$ NCs (about 10 nm), which were considered to be the two most efficient UC host lattices with small particle size for a long time, were synthesized by solvothermal process. In addition, the doping levels of lanthanide ions of YF_3 and α-$NaYF_4$ NCs are the same as LuF_3 NCs. The XRD patterns, TEM images and UC spectra of them are shown in Fig. S2, Fig. S3, Fig. S4 and Fig. 2, respectively. By integrating the intensities of UC spectra shown in Fig. 2, we obtained that the green UC emission of LuF_3 NCs is 18.7 times and 5.1 times stronger than that of YF_3 and α-$NaYF_4$ NCs respectively; the red UC emission of LuF_3 NCs is 13.2 times and 0.6 times stronger than that of YF_3 and α-$NaYF_4$ NCs respectively. These data prove that LuF_3 is an efficient UC host lattices with small particle size.

Fig. 3 is the decay curves of LuF_3: 20% Yb^{3+}, 2% Er^{3+} NCs under the 980 nm excitation wavelength. Under 980 nm excitation wavelength, the decay curves for $^4S_{3/2} \rightarrow {}^4I_{15/2}$ transition and $^4F_{9/2} \rightarrow {}^4I_{15/2}$ transition exhibit a single exponential function. The high concentration of Yb^{3+} ions (20 mol%) is considered as the main factor for explaining this phenomenon. Excited by 980 nm wavelength, Yb^{3+} ions continuously absorb 980 nm photons and the energy migrations among Yb^{3+} ions are very fast due to the high Yb^{3+} ions concentration. Therefore, the Yb^{3+} ions, which are closed to the Er^{3+} ions, can assist the Yb^{3+} ions far from the Er^{3+} ions to transfer their energy to the Er^{3+} ions. So the decay curves for the $^4S_{3/2} \rightarrow {}^4I_{15/2}$ transition and $^4F_{9/2} \rightarrow {}^4I_{15/2}$ transition in the NCs excited by 980 nm wavelength exhibit a single exponential function. The lifetimes of $^4S_{3/2} \rightarrow {}^4I_{15/2}$ transition and $^4F_{9/2} \rightarrow {}^4I_{15/2}$ transition are 103.4 μs and 238 μs respectively, obtained by integrating the area under the corresponding decay curves with the normalized initial intensity. Since the decay time of the $^4S_{3/2} \rightarrow {}^4I_{15/2}$ transition is approximately half of the $^4F_{9/2} \rightarrow {}^4I_{15/2}$ transition, it can conclude that the population of $^4F_{9/2}$ level mainly originates from $^4I_{13/2}$ level, not from $^2H_{11/2}/^4S_{3/2}$ level. The explanation of this phenomenon has been reported in our previous article [39].

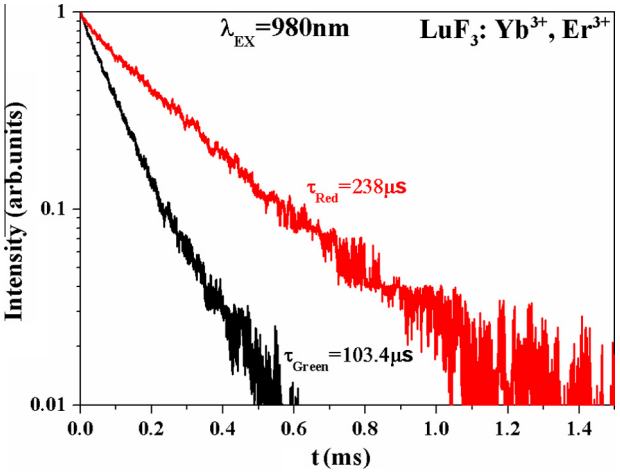

Fig. 3. The decay curves for $^4S_{3/2} \rightarrow {}^4I_{15/2}$ transition and $^4F_{9/2} \rightarrow {}^4I_{15/2}$ transition in LuF_3: Yb^{3+}, Er^{3+} NCs under 980 nm excitation wavelength.

To determine the number of the photons involved in populating the $^2H_{11/2}/^4S_{3/2}$ and $^4F_{9/2}$ states, the pump power dependence of the UC intensity of LuF_3: 20% Yb^{3+}, 2% Er^{3+} NCs has been investigated, as shown in Fig. 4. The UC luminescence intensity (I) is related to the pump intensity (P) via the formula $I \propto P^n$, where n is the number of the photons required to populate the emitting level and can be determined from the slope of the linear plots between *log(I)* and *log(P)*. The slopes for the green and red emission are all close to 2 at relatively low power density, indicating a two-photon process for them. In theory, the slopes (n) for the green and red UC emission should be integer 2 for a two-photon UC process. However, the thermal effect would lead to the quenching of UC emission, resulting in the decrease of the slopes in general. Since the excitation power density was high enough, the strong near infrared photons absorption caused the temperature increase at the irradiated region of the testing samples, inducing the thermal effect [36]. The existence of the thermal effect can be proved by the ratio of $^2H_{11/2} \rightarrow {}^4I_{15/2}$ transition to $^4S_{3/2} \rightarrow {}^4I_{15/2}$ transition, which will be presented in the following paragraph. If the thermal effect could be avoided, the slopes should be larger than the present experimental values. At high power density, the slopes of the curves are reduced due to the saturation effect, as predicated by Pollnau et al. earlier [37].

Fig. 5 shows the dependence of the intensity ratio of $^2H_{11/2} \rightarrow {}^4I_{15/2}$ to $^4S_{3/2} \rightarrow {}^4I_{15/2}$ (R_{HS}) as well as $^4F_{9/2} \rightarrow {}^4I_{15/2}$ to $^2H_{11/2}/^4S_{3/2} \rightarrow {}^4I_{15/2}$ (R_{RG}) upon the pump power. The total changing trend of R_{HS} and R_{RG} are both upward with the increasing pump power. In fact, a thermal equilibrium exists between $^2H_{11/2}$ and $^4S_{3/2}$ energy levels of Er^{3+} ions, owing to the narrow energy gap between them. According to Boltzmann's distribution, the intensity ratio (R_{HS}) between $^2H_{11/2} \rightarrow {}^4I_{15/2}$ transition and $^4S_{3/2} \rightarrow {}^4I_{15/2}$ transition as a function of temperature can be expressed as:

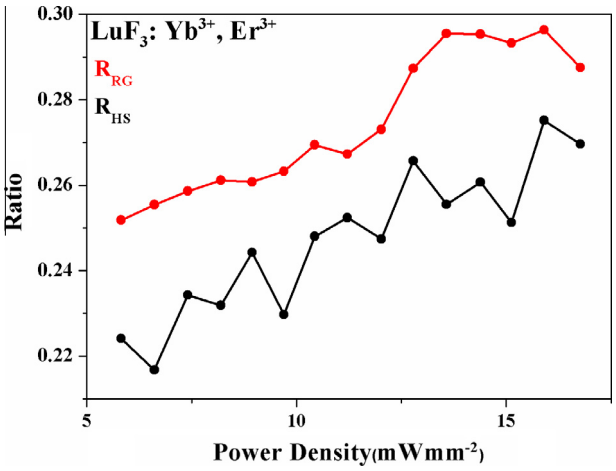

Fig. 5. The intensity ratio of $^2H_{11/2} \rightarrow {}^4I_{15/2}$ to $^4S_{3/2} \rightarrow {}^4I_{15/2}$ and $^4F_{9/2} \rightarrow {}^4I_{15/2}$ to $^2H_{11/2}/^4S_{3/2} \rightarrow {}^4I_{15/2}$ as a function of excitation power.

$$R_{HS} = Ce^{-\Delta E/kT}. \quad (1)$$

Here ΔE is the energy distance between $^2H_{11/2}$ and $^4S_{3/2}$ energy levels, k is the Boltzmann constant, T is absolute temperature and C is a constant. According to Eq. (1), we can derive

$$\ln(1/R_{HS}) = C\Delta E/kT. \quad (2)$$

Considering the total changing trend of R_{HS} is upward with the increasing pump power, it can conclude that the changing trend of the temperature (T) is also upward with the increasing pump power. This provide a clear evidence for the existence of the thermal effect. Meanwhile, it can also explain the changing of R_{RG} dependent on the pump power. As the temperature is increased, the nonradiative relaxation from $^2H_{11/2}/^4S_{3/2}$ to $^4F_{9/2}$ become more effective, resulting in the increase of R_{RG} with the increasing pump power [38].

The energy level diagram including various mainly UC mechanisms is shown in Fig. 6. Excited by 980 nm wavelength, Yb^{3+} ions are excited to $^2F_{5/2}$ level by ground state absorption (GSA). Then the Er^{3+} ions in the ground state, $^4I_{15/2}$ level, can be excited to the $^4I_{11/2}$ level by taking the energy from the excited Yb^{3+} ions (ET1). Subsequently, the higher $^4F_{7/2}$ energy level of Er^{3+} can be populated by ET2 from $^4I_{11/2}$ level. The Er^{3+} ions in $^4F_{7/2}$ energy level can then relax nonradiatively by a fast multiphoton decay process to the $^2H_{11/2}$ and $^4S_{3/2}$ levels, and the dominant green UC emissions occur. Alternatively, the Er^{3+} ions in $^2H_{11/2}$ and $^4S_{3/2}$ levels can further relax and populate the $^4F_{9/2}$ level. Moreover, the population of $^4F_{9/2}$ level also can be through the nonradiative relaxation processes from $^4I_{11/2}$ level to $^4I_{13/2}$ level and subsequent ET(3) processes. The populated $^4F_{9/2}$ level of the Er^{3+} ions mainly relaxes radiatively to the ground state $^4I_{15/2}$ level, which causes the red UC emissions.

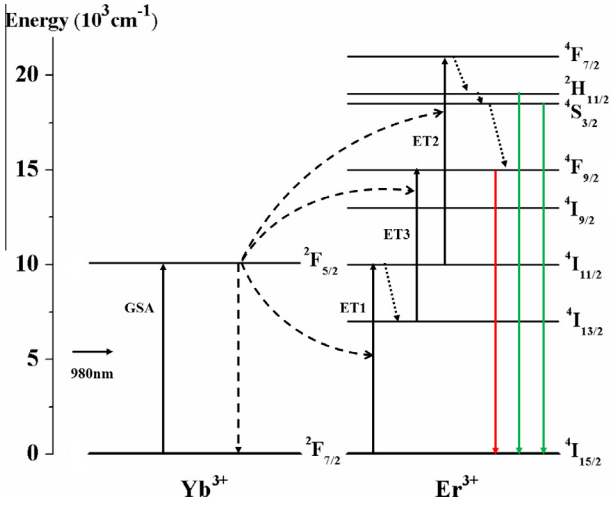

Fig. 6. The energy level diagrams and dominant UC mechanisms in LuF_3: Yb^{3+}, Er^{3+} NCs following 980 nm excitation.

4. Conclusions

In summary, about 10 nm orthorhombic LuF_3: Yb^{3+}, Er^{3+} rectangular NCs were synthesized by a facile and effective solvothermal process. Compared with YF_3 and α-$NaYF_4$ NCs, owning the similar size and the same doping levels of Yb^{3+} ions and Er^{3+} ions as LuF_3 NCs, the green UC emission of LuF_3 NCs is 18.7 times and 5.1 times stronger than that of YF_3 and α-$NaYF_4$ NCs respectively; the red UC emission of LuF_3 NCs is 13.2 times and 0.6 times stronger than that of YF_3 and α-$NaYF_4$ NCs respectively. Excited by 980 nm wavelength, the decay curves of both $^4S_{3/2} \rightarrow {}^4I_{15/2}$ transition and $^4F_{9/2} \rightarrow {}^4I_{15/2}$ transition exhibit a single exponential function, caused by the high concentration of Yb^{3+} ions (20 mol%). Moreover, both the green and red UC emissions are two-photon processes. However, the slopes of the linear plots between *log(I)* and *log(P)* for green UC and red UC are all less than 2, which is due to the thermal effect. In addition, utilizing the pump power dependence of the intensity ratio of $^2H_{11/2} \rightarrow {}^4I_{15/2}$ transition to $^4S_{3/2} \rightarrow {}^4I_{15/2}$ transition, we proved the existence of the thermal effect.

Acknowledgments

This work is financially supported by the National Natural Science Foundation of China (51172226, 61275055, 11274007, 11174278, 51402284, 11474035), the Natural Science Foundation of Jilin province (201205024, 20140101169JC) and the Youth Foundation of Jilin Province (20150520022JH).

Appendix A. Supplementary material

Supplementary data associated with this article can be found, in the online version, at http://dx.doi.org/10.1016/j.jcis.2015.08.026.

References

[1] D.K. Chatterjee, M.K. Gnanasammandhan, Y. Zhang, Small 24 (2010) 2781–2795.
[2] G.F. Wang, Q. Peng, Y.D. Li, Acc. Chem. Res. 44 (2011) 322–332.
[3] E.M. Dianov, Light: Sci. Appl. 1 (2012) e12.
[4] W.P. Qin, Z.Y. Liu, C.N. Sin, C.F. Wu, G.S. Qin, Z. Chen, K.Z. Zheng, Light: Sci. Appl. 3 (2014) e193.
[5] J.H. Zhang, Z.D. Hao, J. Li, X. Zhang, Y.S. Luo, G.H. Pan, Light: Sci. Appl. 4 (2015) e239.
[6] Z.N. Wu, C.R. Guo, S. Liang, H. Zhang, L.P. Wang, H.C. Sun, B. Yang, J. Mater. Chem. 22 (2012) 18596–18602.
[7] S.S. Cui, H.Y. Chen, H.Y. Zhu, J.M. Tian, X.M. Chi, Z.Y. Qian, S. Achilefuc, Y.Q. Gu, J. Mater. Chem. 22 (2012) 4861–4873.
[8] G.C. Jiang, J. Pichaandi, N.J.J. Johnson, R.D. Burke, F.C.J.M. van Veggel, Langmuir 28 (2012) 3239–3247.
[9] F. Shi, J.S. Wang, D.S. Zhang, G.S. Qin, W.P. Qin, J. Mater. Chem. 21 (2011) 13413–13421.
[10] Z.L. Wang, J.H. Hao, H.L.W. Chan, G.L. Law, W.T. Wong, K.L. Wong, M.B. Murphy, T. Su, Z.H. Zhang, S.Q. Zeng, Nanoscale 3 (2011) 2175–2181.
[11] R.A. Jalil, Y. Zhang, Biomaterials 29 (2008) 4122–4128.
[12] Z.Q. Li, Y. Zhang, S. Jiang, Adv. Mater. 20 (2008) 4765–4769.
[13] H.X. Mai, Y.W. Zhang, L.D. Sun, C.H. Yan, J. Phys. Chem. C 111 (2007) 13721–13729.
[14] M.X. Yu, F.Y. Li, Z.G. Chen, H. Hu, C. Zhan, H. Yang, C.H. Huang, Anal. Chem. 81 (2009) 930–935.
[15] J. Zhou, X.J. Zhu, M. Chen, Y. Sun, F.Y. Li, Biomaterials 33 (2012) 6201–6210.

[16] F. Shi, J.S. Wang, X.S. Zhai, D. Zhao, W.P. Qin, CrystEngComm 13 (2011) 3782–3787.
[17] Q.M. Huang, J.C. Yu, E. Ma, K.M. Lin, J. Phys. Chem. C 114 (2010) 4719–4724.
[18] Y. Wei, F.Q. Lu, X.R. Zhang, D.P. Chen, Chem. Mater. 18 (2006) 5733–5737.
[19] H.X. Mai, Y.W. Zhang, L.D. Sun, C.H. Yan, J. Phys. Chem. C 111 (2007) 13730–13739.
[20] K.W. Krämer, D. Biner, G. Frei, H.U. Güdel, M.P. Hehlen, S.R. Lüthi, Chem. Mater. 16 (2004) 1244–1251.
[21] T.S. Yang, Y. Sun, Q. Liu, W. Feng, P.Y. Yang, F.Y. Li, Biomaterials 33 (2012) 3733–3742.
[22] Z.Q. Li, Y. Zhang, Nanotechnology 19 (2008) 345606–345610.
[23] G.S. Yi, G.M. Chow, J. Mater. Chem. 15 (2005) 4460–4464.
[24] Q. Liu, Y. Sun, T.S. Yang, W. Feng, C.G. Li, F.Y. Li, J. Am. Chem. Soc. 133 (2011) 17122–17125.
[25] X.J. Zhu, J. Zhou, M. Chen, M. Shi, W. Feng, F.Y. Li, Biomaterials 33 (2012) 4618–4627.
[26] B.S. Cao, Y.Y. He, L. Zhang, B. Dong, J. Lumin. 135 (2013) 128–132.
[27] Y. Sun, J.J. Peng, W. Feng, F.Y. Li, Theranostics 3 (2013) 346–353.
[28] D.Q. Chen, Y.L. Yu, F. Huang, Y.S. Wang, Chem. Commun. 47 (2011) 2601–2603.
[29] R. Kumar, M. Nyk, T.Y. Ohulchanskyy, C.A. Flask, P.N. Prasad, Adv. Funct. Mater. 19 (2009) 853–859.
[30] G.S. Yi, G.M. Chow, Chem. Mater. 19 (2007) 341–343.
[31] Z.G. Chen, H.L. Chen, H. Hu, M.X. Yu, F.Y. Li, Q. Zhang, Z.G. Zhou, T. Yi, C.H. Huang, J. Am. Chem. Soc. 130 (2008) 3023–3029.
[32] G.Y. Chen, H.L. Qiu, R.W. Fan, S.W. Hao, S. Tan, C.H. Yang, G. Han, J. Mater. Chem. 22 (2012) 20190–20196.
[33] E.J. He, H.R. Zheng, W. Gao, Y.X. Tu, Y. Lu, G.A. Li, Mater. Res. Bull. 48 (2013) 3505–3512.
[34] Y.P. Li, J.H. Zhang, Y.S. Luo, X. Zhang, Z.D. Hao, X.J. Wang, J. Mater. Chem. 21 (2011) 2895–2900.
[35] O. Guillot-Noel, B. Bellamy, B. Viana, D. Gourier, Phys. Rev. B 60 (1999) 1668–1677.
[36] X. Bai, H.W. Song, G.H. Pan, Y.Q. Lei, T. Wang, X.G. Ren, S.Z. Lu, B. Dong, Q.L. Dai, L.B. Fan, J. Phys. Chem. C 111 (2007) 13611–13617.
[37] M. Pollnau, D.R. Gamelin, S.R. Lüthi, H.U. Güdel, M.P. Hehlen, Phys. Rev. B 61 (2000) 3337–3346.
[38] G.F. Wang, Q. Peng, Y.D. Li, J. Am. Chem. Soc. 131 (2009) 14200–14201.
[39] G.T. Xiang, J.H. Zhang, Z.D. Hao, X. Zhang, Y.S. Luo, S.Z. Lü, H.F. Zhao, CrystEngComm 16 (2014) 2499–2507.